Bright and dark plasmon resonances of nanoplasmonic antennas evanescently coupled with a silicon nitride waveguide

Frédéric Peyskens,[1,2,*] **Ananth Z. Subramanian,**[1,2] **Pieter Neutens,**[3,4] **Ashim Dhakal,**[1,2] **Pol Van Dorpe,**[3,4] **Nicolas Le Thomas**[1,2] **and Roel Baets**[1,2]

[1]*Photonics Research Group, INTEC Department, Ghent University-imec, Sint-Pietersnieuwstraat 41, 9000 Ghent, Belgium.*
[2]*Center for Nano- and Biophotonics, Ghent University, Belgium.*
[3]*IMEC, Kapeldreef 75, 3001 Heverlee, Belgium.*
[4]*Department of Physics, Celestijnenlaan 200D, 3001 Leuven, Belgium*
[*]*fpeysken@intec.ugent.be*

Abstract: In this work we investigate numerically and experimentally the resonance wavelength tuning of different nanoplasmonic antennas excited through the evanescent field of a single mode silicon nitride waveguide and study their interaction with this excitation field. Experimental interaction efficiencies up to 19% are reported and it is shown that the waveguide geometry can be tuned in order to optimize this interaction. Apart from the excitation of bright plasmon modes, an efficient coupling between the evanescent field and a dark plasmonic resonance is experimentally demonstrated and theoretically explained as a result of the propagation induced phase delay.

OCIS codes: (250.5300) Photonic integrated circuits; (250.5403) Plasmonics; (220.4241) Nanostructure fabrication; (230.7370) Waveguides.

References and links

1. J. N. Anker, W. P. Hall, O. Lyandres, N. C. Shah, J. Zhao, and R.P. Van Duyne, "Biosensing with plasmonic nanosensors," Nat. Mater. **7**, 442–453 (2008).
2. K. A. Willets, and R.P. Van Duyne, "Localized surface plasmon resonance spectroscopy and sensing," Annu. Rev. Phys. Chem. **58**, 267–297 (2007).
3. N. J. Halas, S. Lal, W-S. Chang, S. Link, and P. Nordlander, "Plasmons in strongly coupled metallic nanostructures," Chem. Rev. **111**, 3913–3961 (2011).
4. K. M. Mayer, and J.H. Hafner, "Localized surface plasmon resonance sensors," Chem. Rev. **111**, 3828–3857 (2011).
5. K. L. Kelly, E. Coronado, L. L. Zhao, and G. C. Schatz, "The optical properties of metal nanoparticles: the influence of size, shape, and dielectric environment," J. Phys. Chem. B **111**(3), 668–677 (2003).
6. A. Sundaramurthy, K. B. Crozier, G. S. Kino, D. P. Fromm, P. J. Schuck, and W. E. Moerner, "Field enhancement and gap-dependent resonance in a system of two opposing tip-to-tip Au nanotriangles," Phys. Rev. B **72**, 165409-1–165409-6 (2005).
7. H. Fischer, and O. J. F. Martin, "Engineering the optical response of plasmonic nanoantennas," Opt. Express **16**(12), 9144–9154 (2008).
8. V. Giannini, A. I. Fernández-Domínguez, S. C. Heck, and S. A. Maier, "Plasmonic nanoantennas: fundamentals and their use in controlling the radiative properties of nanoemitters," Chem. Rev. **111**, 3888–3912 (2011).
9. J. J. Mock, D. R. Smith, and S. Schultz, "Local refractive index dependence of plasmon resonance spectra from individual nanoparticles," Nano Lett. **3**(4), 485–491 (2003).

#228908 - $15.00 USD Received 5 Dec 2014; revised 18 Jan 2015; accepted 22 Jan 2015; published 2 Feb 2015

10. T. R. Jensen, M. Duval Malinsky, C. L. Haynes, and R. P. Van Duyne, "Nanosphere lithography: tunable localized surface plasmon resonance spectra of silver nanoparticles," J. Phys. Chem. B **104**, 10549–10556 (2000).
11. K.-H. Su, Q.-H. Wei, X. Zhang, J. J. Mock, D. R. Smith, and S. Schultz, "Interparticle coupling effects on plasmon resonances of nanogold particles," Nano Lett. **3**(8), 1087–1090 (2003).
12. O. L. Muskens, V. Giannini, J. A. Sánchez-Gil, and J. Gómez Rivas, "Optical scattering resonances of single and coupled dimer plasmonic nanoantennas," Opt. Express **15**(26), 17736–17746 (2007).
13. A. J. Haes, S. Zou, G. C. Schatz, and R. P. Van Duyne, "Nanoscale optical biosensor: short range distance dependence of the localized surface plasmon resonance of noble metal nanoparticles," J. Phys. Chem. B **108**, 6961–6968 (2004).
14. A. J. Haes, W. P. Hall, L. Chang, W. L. Klein, and R. P. Van Duyne, "A localized surface plasmon resonance biosensor: first steps toward an assay for Alzheimers disease," Nano Lett. **4**(6), 1029–1034 (2004).
15. N. Verellen, P. Van Dorpe, C. Huang, K. Lodewijks, G. A. E. Vandenbosch, L. Lagae, and V. V. Moshchalkov, "Plasmon line shaping using nanocrosses for high sensitivity localized surface plasmon resonance sensing," Nano Lett. **11**, 391–397 (2011).
16. A. Kinkhabwala, Z. Yu, S. Fan, Y. Avlasevich, K. Müllen, and W. E. Moerner, "Large single-molecule fluorescence enhancements produced by a bowtie nanoantenna," Nature Photon. **3**, 654–657 (2009).
17. Y. Chu, M. G. Banaee, and K. B. Crozier, "Double-resonance plasmon substrates for surface-enhanced Raman scattering with enhancement at excitation and Stokes frequencies," ACS Nano **4**(5), 2804–2810 (2010).
18. A. D. McFarland, M. A. Young, J. A. Dieringer, and R. P. Van Duyne, "Wavelength-scanned surface-enhanced Raman excitation spectroscopy," J. Phys. Chem. B **109**, 11279–11285 (2005).
19. L. Novotny, and N. van Hulst, "Antennas for light," Nature Photon. **5**, 83–90 (2011).
20. T. J. Seok, A. Jamshidi, M. Eggleston, and M. C. Wu, "Mass-producible and efficient optical antennas with CMOS-fabricated nanometer-scale gap," Opt. Express **21**(14), 16561–16569 (2013).
21. L. Arnaud, A. Bruyant, M. Renault, Y. Hadjar, R. Salas-Montiel, A. Apuzzo, G. Lérondel, A. Morand, P. Benech, E. Le Coarer, and S. Blaize, "Waveguide-coupled nanowire as an optical antenna," J. Opt. Soc. Am. A **30**(11), 2347–2355 (2013).
22. F. B. Arango, A. Kwadrin, and A. F. Koenderink, "Plasmonic antennas hybridized with dielectric waveguides," ACS Nano **6**(11), 10156–10167 (2012).
23. M. Février, P. Gogol, A. Aassime, R. Mégy, C. Delacour, A. Chelnokov, A. Apuzzo, S. Blaize, J-M. Lourtioz, and B. Dagens, "Giant coupling effect between metal nanoparticle chain and optical waveguide," Nano Lett. **12**, 1032–1037 (2012).
24. M. Février, P. Gogol, J-M. Lourtioz, and B. Dagens, "Metallic nanoparticle chains on dielectric waveguides: coupled and uncoupled situations compared," Opt. Express **21**(21), 24504–24513 (2013).
25. M. Février, P. Gogol, G. Barbillon, A. Aassime, R. Mégy, B. Bartenlian, J-M. Lourtioz, and B. Dagens, "Integration of short gold nanoparticles chain on SOI waveguide toward compact integrated bio-sensors," Opt. Express **20**(16), 17402–17410 (2012).
26. M. Chamanzar, Z. Xia, S. Yegnanarayanan, and A. Adibi, "Hybrid integrated plasmonic-photonic waveguides for on-chip localized surface plasmon resonance (LSPR) sensing and spectroscopy," Opt. Express **21**(26), 32086–32098 (2013).
27. A.Z. Subramanian, P. Neutens, A. Dhakal, R. Jansen, T. Claes, X. Rottenberg, F. Peyskens, S. Selvaraja, P. Helin, B. Du Bois, K. Leyssens, S. Severi, P. Deshpande, R. Baets, and P. Van Dorpe, "Low-loss singlemode PECVD silicon nitride photonic wire waveguides for 532900 nm wavelength window fabricated within a CMOS pilot line," IEEE Photon. J. **5**(6), 1943–0655 (2013).
28. S. Romero-García, F. Merget, F. Zhong, H. Finkelstein, and J. Witzens, "Silicon nitride CMOS-compatible platform for integrated photonics applications at visible wavelengths," Opt. Express **21**(12), 14036–14046 (2013).
29. A. Dhakal, A.Z. Subramanian, P. Wuytens, F. Peyskens, N. Le Thomas, and R. Baets, "Evanescent excitation and collection of spontaneous Raman spectra using silicon nitride nanophotonic waveguides," Opt. Lett. **39**(13), 4025–4028 (2014).
30. P.B. Johnson, and R.W. Christy, "Optical constants of the noble metals," Phys. Rev. B **6**(12), 4370–4379 (1972).
31. W. M. Haynes, ed., *CRC Handbook of Chemistry and Physics* 95th Edition (Internet Version 2015) (CRC/Taylor and Francis, 2015).
32. M. Bosman, L. Zhang, H. Duan, S. Fen Tan, C. A. Nijhuis, C.W. Qiu, and J. K. W. Yang, "Encapsulated annealing: enhancing the plasmon quality factor in lithographically-defined nanostructures," Sci. Rep. **4**, 5537 (2014).
33. T. Siegfried, Y. Ekinci, O.J.F. Martin, and H. Sigg, "Engineering metal adhesion layers that do not deteriorate plasmon resonances," ACS Nano **7**(3), 2751–2757 (2013).
34. N. Verellen, P. Van Dorpe, D. Vercruysse, G.A.E. Vandenbosch, and V. V. Moshchalkov, "Dark and bright localized surface plasmons in nanocrosses," Opt. Express **19**(12), 11034–11051 (2011).

#228908 - $15.00 USD Received 5 Dec 2014; revised 18 Jan 2015; accepted 22 Jan 2015; published 2 Feb 2015

1. Introduction

Plasmonic nanostructures have attracted much interest in the world of biosensing due to their remarkable light enhancement capabilities and extreme sensitivity to local environmental changes. These properties emerge as a result of the collective oscillation of conduction electrons (plasmons) upon light excitation. [1–4] The plasmon resonance frequency can be tuned by varying the nanoparticle's size, shape, composition and dielectric surroundings [1–12] and a broad range of biological and chemical applications stems from these spectral tuning capabilities. [13–18] The dependence of the localized surface plasmon resonance (LSPR) on the refractive index has for example been used in LSPR sensing to monitor molecular binding events. [14] Furthermore it is known that the near-field coupling between individual nanoparticles leads to the formation of highly localized and intense regions in the gaps between these particles (hotspots) which can be used to enhance extremely weak Raman signals through Surface Enhanced Raman Spectroscopy (SERS). [1]

Several methods have been applied to fabricate such plasmonic nanostructures. [8–12, 19] Bottom-up strategies, such as chemical synthesis or colloidal lithography allow the production of a large number of nanoparticles in a variety of sizes and shapes. [8–10] Arranging colloidal particles to produce a specific nanoparticle geometry is still a challenge however. [19] Top-down approaches, such as e-beam lithography or focused ion beam milling, on the other hand do not involve chemical synthesis or self-assembly and can be used to pattern complicated shapes very accurately at a certain position on a substrate albeit at a high cost and low throughput. [8, 11, 12] Moreover, deep-UV spacer lithography can be used to fabricate arrays of sub 10 nm gap nanostructures in a highly controllable and reproducible way. [20]

Most of this research is focused on the fabrication of nanoplasmonic antennas on top of general substrates. In such cases large and expensive free-space optics is required for both excitation and collection of the signals. Recently the integration of metallic nanoparticles on top of photonic integrated circuits (PICs) has been investigated. [21–26] The fundamental building block of these circuits is a (single-mode) waveguide in which light is guided in a high-index core material surrounded by lower-index materials. In [21] a low index contrast waveguide is considered and in all cases the antenna geometry consisted of a single element antenna [21] or chains of (coupled) single element antennas (such as Yagi-Uda antennas [22] or single rod antennas [23–26]). In such a hybrid on-chip platform the antennas are excited through the sub-wavelength evanescent tail of the waveguide mode and can be aligned with the polarization of the input beam by fabrication. This allows an optimal excitation of the plasmon resonance since it is highly dependent on the input polarization. It has been shown that such on-chip antennas can efficiently couple a diffraction-limited beam into the waveguide mode [22] and could also be used for highly sensitive LSPR applications. [25, 26] Since thousands of such sensing devices can be packed on a single chip of a few square millimeter and can be mass-produced using CMOS-compatible technology, this platform offers a versatile and low-cost alternative for the commonly used bulky and expensive free-space optics systems.

A comparative study of the resonance wavelength behaviour on different geometrical antenna parameters upon evanescent waveguide excitation and the integration of narrow gap plasmonic nanostructures on a PIC has not been demonstrated so far. In this work we present a theoretical and experimental study of three widely used antenna types (single rod, double rod and bowtie antenna) fabricated on top of a single mode silicon nitride Si_3N_4 waveguide and resonant in the near-IR region (700-1000 nm) because most biological applications require visible and near-IR wavelenghts for which Si_3N_4 (as opposed to Si) has a high transparency. [27, 28] The near-IR region is of particular interest for on-chip Raman spectroscopy as pumping in the near-IR (e.g. at 785 nm) can reduce the unwanted fluorescence background and allows low-loss propagation of both pump and Stokes light in a Si_3N_4 waveguide. [27–29] For this wavelength

#228908 - $15.00 USD Received 5 Dec 2014; revised 18 Jan 2015; accepted 22 Jan 2015; published 2 Feb 2015

range, there are also ultra sensitive and low-cost CMOS detectors and imagers available. The spectral response of the dipolar (bright) mode and the interaction of the antennas with the waveguide is investigated. By tuning the bowtie antenna it is furthermore shown experimentally that dark plasmon modes can be efficiently excited through the evanescent waveguide field. These narrow gap nanostructures could be used for on-chip enhanced Raman spectroscopy or improved on-chip LSPR sensing using the multipolar plasmon character.

2. Investigated platform and fabrication details

The platform used in this work is depicted in Fig. 1. It consists of a dielectric waveguide structure and an array of $N = 20$ plasmonic antennas organized in a 1D chain with period $\Lambda = 10\ \mu m$ on top of the waveguide. The fabrication consists of 2 subsequent e-beam lithography steps. We start from a slab wafer of 220 nm PECVD deposited Si_3N_4 on SiO_2 on Si. [27] After a thorough sample clean a Ti adhesion layer ($t_{Ti} \approx 2$ nm) and Au layer ($t_{Au} \approx 35$ nm) are deposited. On top of the Au layer another Ti layer ($t_{Ti}^{top} \approx 2$ nm) is deposited in order to improve the contact with the e-beamresist. In the first e-beam step, the plasmonic antennas are defined in a negative HSQ resist (FOX-12, Dow Corning). After development the samples were etched with a Xe ion miller. In this step it is critical to mill for a sufficiently long time in order to completely remove the unprotected Ti/Au/Ti stack. If not etched properly, the waveguide losses of the eventual device will be very high due to the loss induced by the residual metal. In the second e-beam step the single mode waveguides ($h_{rib} = 220$ nm and $w_{rib} = 700$ nm) are defined in negative ma-N 2403 resist. On top of the ma-N 2403 a very thin e-spacer layer is spun to avoid charging effects during the write process. Such charging effects could lead to large stitching errors and hence increased waveguide losses. The exposed samples are developed with ma-D and etched with an Oxford Plasmalab using a mixture of C_4F_8 and SF_6. Acetone/IPA and an oxygen plasma are used to strip the remaining resist. The best waveguide loss obtained so far with this process is 4 dB/cm (at $\lambda = 785$ nm). In the end, a thin FOX-layer ($t_{FOX} \approx 70$ nm) remains on the top surface of the antenna (which can be removed by a quick HF-dip if necessary). Antenna gaps down to 10 nm were successfully established after ion milling. In the remaining part of the paper we will term waveguides with antennas as patterned waveguides while reference waveguides without antennas will be termed unpatterned. We furthermore compared our 2-step ebeam process (consisting of both Au milling as well as a Si_3N_4 etch) with a 1-step process in which only the Si_3N_4 etch was performed (without metal deposition and milling) and found that the Xe milling has no significant impact on the waveguide loss. AFM images confirm that the roughness of the top surface is almost the same in both cases (≈ 1.39 nm). Despite the fact that an e-spacer was used, we observed with SEM that there were still stitching errors at some locations. These additional scattering centra will increase the waveguide loss. Stitching errors (and sidewall roughness) are therefore considered to be the limiting factors for the waveguide loss in this process.

3. Numerical method and measurement setup

In this section we will outline the numerical method and introduce the measurement setup. The numerical and experimental results will be discussed in the next section. Theoretical extinction spectra of a single antenna are calculated with Lumerical FDTD Solutions. All simulations are performed on a fixed waveguide structure (see Fig. 1(a)) consisting of a Si_3N_4 rib ($h_{rib} = 220$ nm, $w_{rib} = 700$ nm and $n_{rib} = 1.9$) on an SiO_2 undercladding ($n_{uclad} = 1.45$). The refractive index of the top cladding is $n_{tclad} = 1$ (air). The metal stack thicknesses ($t_{Ti} = t_{Ti}^{top} = 2$ nm and $t_{Au} = 35$ nm) are fixed for all antennas (Figs. 1(b)–1(d)) and a built-in refractive index model for Au (Johnson and Christy [30]) and Ti (CRC [31]) is used. The antenna region is meshed with a 2 nm grid and a mesh refinement to 1 nm is applied in the Ti region. The Si substrate is

#228908 - $15.00 USD Received 5 Dec 2014; revised 18 Jan 2015; accepted 22 Jan 2015; published 2 Feb 2015

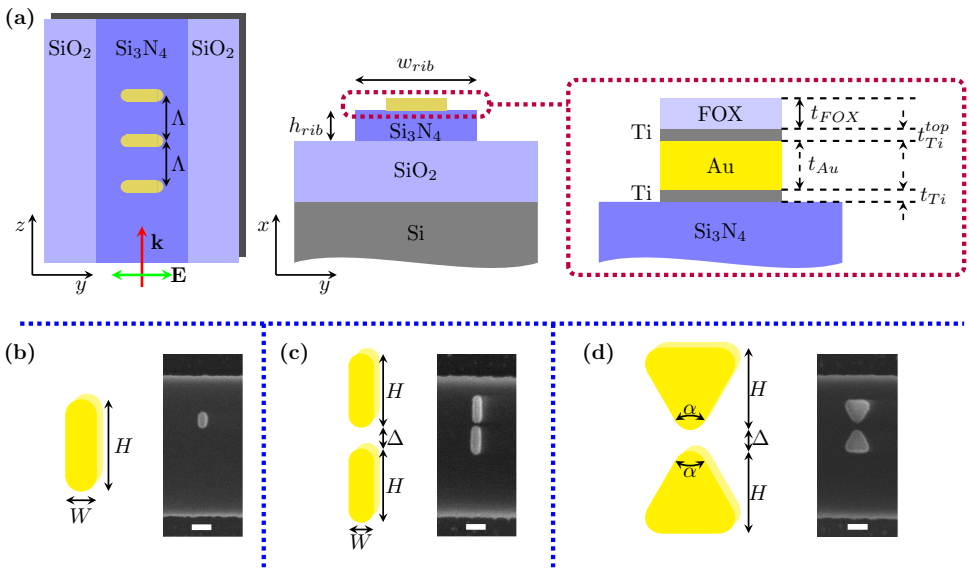

Fig. 1. **On-chip geometry. (a)** Schematic top-view (left) and cross-section (right) of the waveguide geometry. Each waveguide is patterned with an array of $N = 20$ antennas spaced by $\Lambda = 10\ \mu m$. The antennas are excited with a TE-polarized (green arrow) waveguide mode with **k**-vector along the z-direction (red arrow). The stack consists of a Si/SiO_2 substrate and a Si_3N_4 waveguide (height $h_{rib} = 220$ nm and width $w_{rib} = 700$ nm). On top of the Si_3N_4 a Ti/Au/Ti layer is deposited (with thicknesses $t_{Ti}/t_{Au}/t_{Ti}^{top}$). A thin resist layer with thickness t_{FOX} remains at the end of the processing. **(b-d)** Investigated antenna geometries with their corresponding geometrical parameters and a SEM picture of the fabricated structure: **(b)** single rod (SR) antenna with height H and width W, **(c)** double rod (DR) antenna with height H, gap Δ and width W, **(d)** bowtie (BT) antenna with height H, gap Δ and apex angle α. The white scale bar in the SEM pictures equals 100 nm.

not taken into account in the simulation, but for the calculation of the excitation profile this is not necessary since the real oxide cladding is thick enough to avoid substantial power leakage to the Si. The antennas are excited with the evanescent tail of the fundamental TE-mode and transmission spectra are compared in both the unpatterned and patterned case. Single antenna extinction spectra $E(\lambda)$ (in dB) are calculated through $E(\lambda)[dB] = T_{ref}(\lambda)[dB] - T_{ant}(\lambda)[dB]$ in which $T_{ref}(\lambda) = 10\log_{10}(t_{ref}(\lambda))$ is the power transmission of a reference (unpatterned) waveguide (in dB) while $T_{ant} = 10\log_{10}(t_{ant}(\lambda))$ is the power transmission of a patterned waveguide (in dB), so the extinction represents the total transmission loss due to absorption and scattering of the antenna. The interaction efficiency $\eta(\lambda)$ is then defined as the fraction of the power taken away by a single nanoantenna (at wavelength λ) and is calculated through $\eta(\lambda) = 1 - t_{ant}(\lambda)/t_{ref}(\lambda)$. [26]

Transmission spectra of the hybrid waveguides are measured with a horizontal coupling setup as shown in Fig. 2. An NKT EXR-4 Extreme Supercontinuum Source (SC) is coupled to a splitter module (NIRF), which transmits light in a wavelength band between 600 nm and 1120 nm. The fiber coupled (FC) light is then converted to a free space beam by an achromatic fiber collimator (C) and sent through a free-space broadband polarizer (P) to convert the unpolarized beam into a TE-beam after which the light is fiber coupled again to a lensed fiber. The same configuration is used at the output in order to extract the TE component of the transmitted light. The piezocontroller (XYZ) is applied to achieve maximal coupling between the lensed fibers

#228908 - $15.00 USD Received 5 Dec 2014; revised 18 Jan 2015; accepted 22 Jan 2015; published 2 Feb 2015

and the facets of the chip. The spectra are then recorded with an Advantest Optical Spectrum Analyzer (OSA). The inset figure depicts the scattering of an array of antennas.

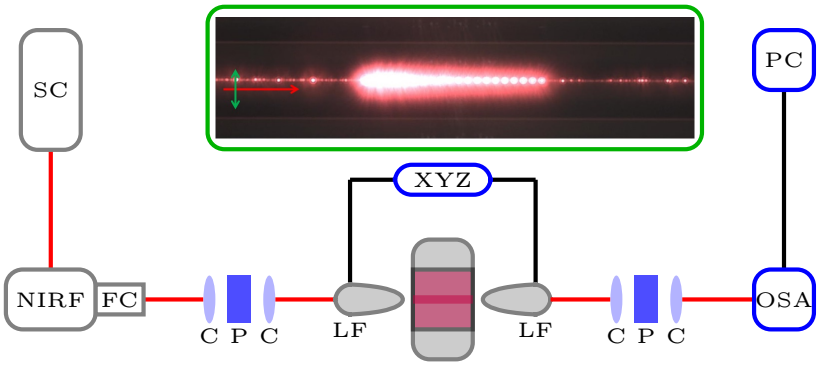

Fig. 2. **Measurement setup.** SC: supercontinuum source, NIRF: near-IR filter, FC: fiber coupling unit, C: achromatic fiber collimator, P: free-space broadband polarizer, LF: lensed fiber, XYZ: piezo controller stage, OSA: Optical Spectrum Analyzer, PC: OSA control using Python based measurement framework. Inset: scattering of an on-chip array of antennas. The red arrow depicts the propagation direction of the light while the green arrow represents the polarization state.

The experimental extinction $E(\lambda)$ of a single nanoantenna is calculated using the following approximate formula $E(\lambda)[dB] = (T_{ref}(\lambda)[dB] - T_{Nant}(\lambda)[dB])/N$, in which the power transmission of the patterned waveguide (T_{Nant}) now contains the contributions of all N antennas. Due to the large spacing Λ there is a negligible near-field coupling between two consecutive antennas as opposed to the near-field coupling between the elements of a single antenna in case of gapped nanostructures. The antenna array forms a periodic medium however, so a diffractive coupling between the forward and backward propagating modes at discrete λ is expected, which will translate in a periodic ripple on the overall extinction. Since the light decays exponentially, the approximate formula will however give the correct experimental single antenna extinction.

4. Discussion of bright mode resonance behaviour

In Fig. 3 both the theoretical and experimental extinction spectra are shown. Each spectrum is normalized with its own maximum and shifted with respect to the previous spectrum for improved visualization. Both the theoretical and experimental single rod (SR) spectra are shifted with steps of 0.5. The theoretical double rod (DR) and bowtie (BT) spectra for different H are shifted with 1.5 while for a fixed H the shift between different Δ curves is 0.1. For the experimental DR and BT spectra, the shift between different H curves is 2.5 and for a fixed H the shift between different Δ curves is 0.3. Hence the relative normalized extinction is shown in all subplots of Fig. 3. The theoretical curves depict the response of a single rod (a), a double rod (b) and a bowtie antenna (c) respectively under changes in their geometrical parameters. In case of the SR and DR antennas a fixed antenna width of $W = 55$ nm is chosen based on the SEM pictures of each antenna. For the BT antenna an apex angle $\alpha = 60^\circ$ is chosen. The resonance wavelength of a single rod antenna λ_{res}^{SR} redshifts with increasing rod height H with a sensitivity $S = d\lambda_{res}/dH$ given by $S^{SR} = 3.9$. The resonance wavelength of double rod λ_{res}^{DR} and bowtie λ_{res}^{BT} antennas shows a similar redshift with increasing height but the sensitivity depends

#228908 - $15.00 USD Received 5 Dec 2014; revised 18 Jan 2015; accepted 22 Jan 2015; published 2 Feb 2015

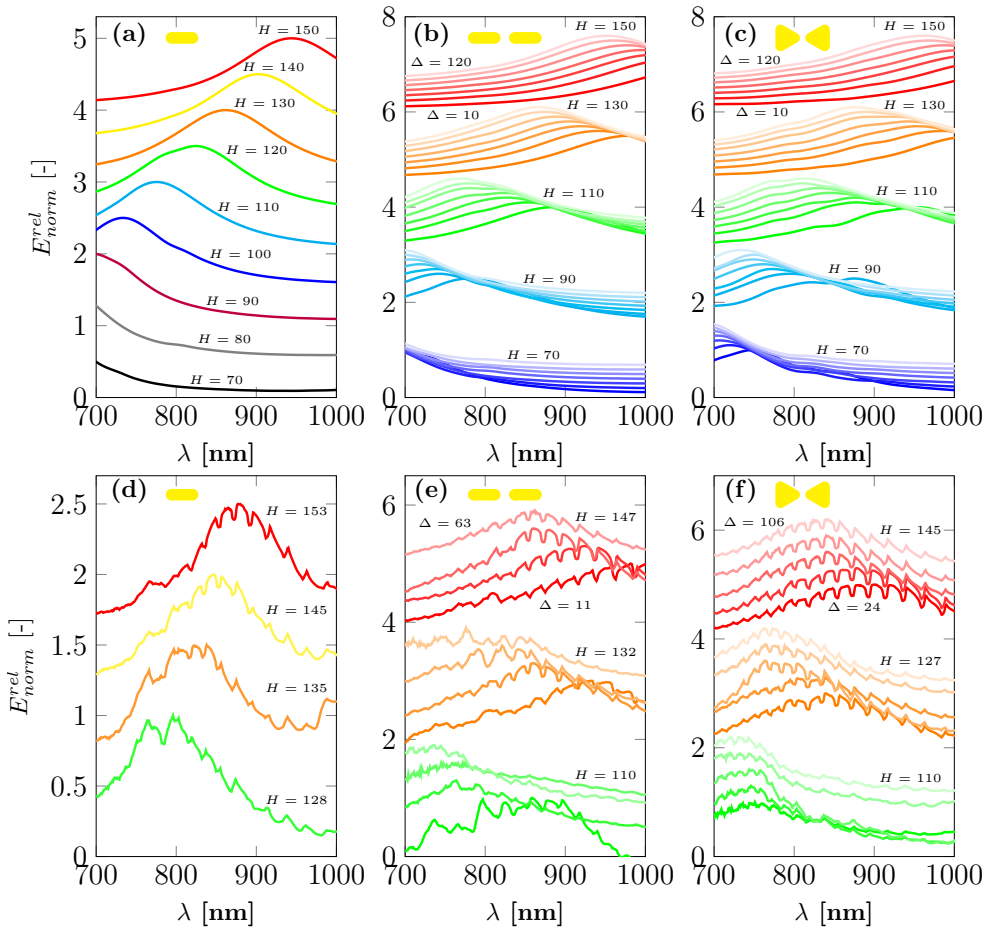

Fig. 3. **Relative Normalized Extinction Curves.** The extinction spectra E^{rel}_{norm} are normalized with their own maximum and then shifted relatively with respect to each other for improved visualization of the resonance wavelength behaviour. **(a-c)** Theoretical spectra of single rod SR **(a)**, double rod DR **(b)** and bowtie BT **(c)** antennas. SR spectra are depicted for different heights H (in nm) and fixed width $W = 55$ nm. For the DR and BT antennas, the spectra are plotted for five different heights H (in nm). For each height, seven different gaps $(10, 20, 30, 40, 60, 90, 120$ nm) are simulated and depicted by the shaded curves in the corresponding height color. The outer right curve of each color corresponds with $\Delta = 10$ nm while the outer left curve corresponds with $\Delta = 120$ nm (see red set of curves). The width of the DR antennas is fixed to $W = 55$ nm and the apex angle of the BT antennas is $\alpha = 60°$. **(d-f)** Experimental spectra of SR **(d)**, DR **(e)** and BT **(f)** antennas. Similar to the theoretical curves, the SR spectra are compared for different heights while the DR and BT spectra are compared for different heights and gaps. The heights and gaps mentioned on the experimental subplots are averages calculated using the measured dimensions (with SEM).

#228908 - $15.00 USD Received 5 Dec 2014; revised 18 Jan 2015; accepted 22 Jan 2015; published 2 Feb 2015

on the gap Δ. DR antennas are more prone to height changes as compared to SR antennas with $S^{DR} = 4.9$ for $\Delta = 10$ nm and $S^{DR} = 4.1$ for $\Delta = 120$ nm. When the gap Δ increases, for a fixed height H, the resonance wavelength λ_{res} blueshifts and will converge for sufficiently large Δ since the individual gold particles decouple and the DR sensitivity will approach that of the SR antennas. Increasing the width W or the gold thickness t_{Au} leads to a blueshift in the spectrum while increasing the thickness of the adhesion layers t_{Ti} and t_{Ti}^{top} results in a redshift. BT antennas are less sensitive to height changes as compared to DR antennas ($S^{BT} = 4.4$ for $\Delta = 10$ nm and $S^{BT} = 3.6$ for $\Delta = 120$ nm). A similar blueshift for increasing Δ (and fixed H) can also be observed. Figures 3(d)–3(f) show the experimentally measured extinction spectra of SR (d), DR (e) and BT (f) antennas (the measured antennas were partially misaligned with respect to the center of the waveguide as can be seen in Figs. 1(b)–1(d)). The measured SR sensitivity is $S^{SR} \approx 3.5$ which deviates about 10% from the theoretically calculated value. For the gapped structures we find $S^{DR} \approx 3.8$ and $S^{BT} \approx 3.34$ (both for a gap of ≈ 60 nm). These values deviate 12% and 12.4% respectively from their numerical estimations. In Fig. 4 we present a comparison between the resonance wavelength tuning predicted by simulation and the experimentally measured resonance wavelengths for SR (Fig. 4(a)), DR (Fig. 4(b)) and BT (Fig. 4(c)) antennas. In each subplot the resonance wavelength is plotted as a function of the antenna height, hence the slope of each curve represents the earlier defined sensitivity S. For the DR and BT antennas, each curve corresponds to a specific gap value. For a fixed height it is clear that the resonance wavelength blueshifts when the gap increases (for DR and BT antennas). The slope (sensitivity) of the experimental data points is in close correspondence with the numerically predicted values. The offset in the absolute position of the resonance wavelength could be ascribed to a variety of factors. Differences between the experimental refractive indices of Au and Ti (due to the specific metal deposition) and the indices used in the simulation, SEM error of the measured antenna dimensions or differences among the $N = 20$ antennas are all possible reasons for this offset. Simulations for SR, DR and BT antennas show that the misalignment of the fabricated antennas with respect to the center of the waveguide has a negligible impact on the precise position of the resonance wavelength.

The fringes superimposed on the broad envelope originate from the gold pattern as they do not appear in the reference waveguide spectrum. As explained in the previous section, a ripple on the extinction is expected due to the fact that the antenna array forms a periodic medium. The distance between two fringes for this 1D grating with period Λ and group index n_g is given by $\lambda^2/(2n_g\Lambda)$ (around a given wavelength λ). In our case the period equals $\Lambda = 10\ \mu m$ and the group index is $n_g \approx 1.936$ (i.e. group index of the waveguide mode at $\lambda = 798$ nm). Theoretically a fringe spacing of 16.45 nm is expected, which is in close correspondence with the experimentally observed fringe spacing (≈ 17 nm for $\lambda = 798$ nm).

The measured Q-factor, calculated using the 3dB-bandwidth of the extinction, of our fabricated devices ranges between ≈ 3.11 and ≈ 7.75 with a typical value of ≈ 5 at $\lambda_{res} = 780$ nm. For pure non-annealed Au antennas (without Ti adhesion layers) $Q-$factors of ≈ 11 (around 780 nm) are experimentally measured. [32] Because we use a Ti adhesion layer on the bottom and top surface the plasmon resonance will broaden and hence reduce the Q-factor as compared to a pure Au antenna. Our simulations show that a 2 nm Ti adhesion layer on the bottom and the top of the Au can easily reduce the Q-factor by 50% (e.g. $Q = 4.5$ versus $Q = 9.3$ for a SR antenna with and without Ti respectively). Local inhomogeneities (such as redeposited Au or small differences among the $N = 20$ antennas) will also contribute to a broadening of the experimental extinction. [26] Reducing the Ti thickness or using a molecular linker adhesion layer can increase the Q-factor again. [33] Another cause of low Q-factors in nanopatterned antennas is polycrystallinity [19]. Recently it has been shown that thermal annealing can increase the Q-factor of lithographically defined structures by reducing the grain boundaries. [32] In that

#228908 - $15.00 USD Received 5 Dec 2014; revised 18 Jan 2015; accepted 22 Jan 2015; published 2 Feb 2015

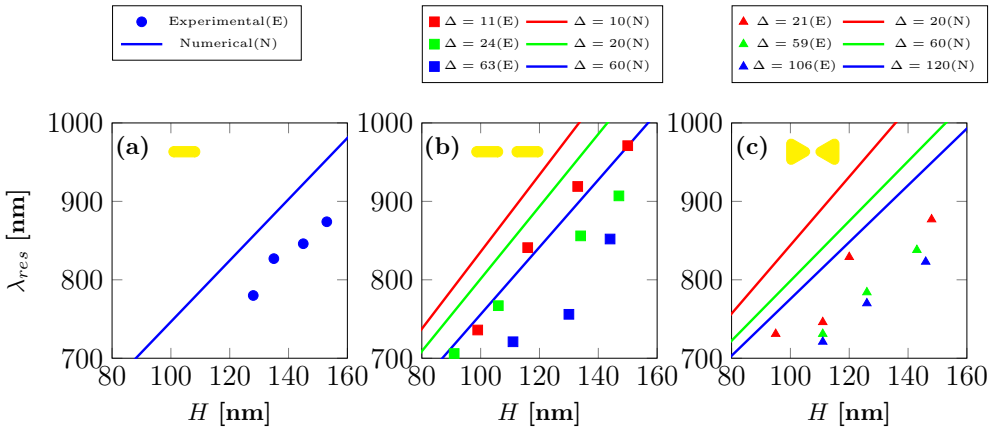

Fig. 4. **Comparison between numerical and experimental results.** Resonance wavelength λ_{res} as a function of the antenna height H for the three antenna geometries. The solid lines represent numerical simulation data while the markers represent experimental data. **(a)** Experimental SR data (circles) compared with simulated data (solid line). **(b)** Experimental DR data (squares) for different gaps Δ (11 nm (red), 24 nm (green), 63 nm (blue)) compared with the simulation data ($\Delta = 10$ nm (red), $\Delta = 20$ nm (green), $\Delta = 60$ nm (blue)). **(c)** Experimental BT data (triangles) for different gaps Δ (21 nm (red), 59 nm (green), 106 nm (blue)) compared with the simulation data ($\Delta = 20$ nm (red), $\Delta = 60$ nm (green), $\Delta = 120$ nm (blue)).

case the antennas have to be encapsulated however to avoid shape changes. [32] The Xe ion milling in our process scheme could, as opposed to procedures based on lift-off, immediately be applied to annealed metal layers in which the nanoantennas can be milled instantly. Since we have shown that the Xe milling has no negative impact on the waveguide loss and allows the fabrication of integrated narrow gap antennas, the suggested scheme could be considered as a proper alternative for lift-off to produce potentially higher Q lithographic antennas.

As we have established the possibility to produce gapped nanostructures on top of a single mode waveguide, it is important to compare the efficiency by which they interact with the evanescent field of the waveguide. This can be quantified by the interaction efficiency $\eta(\lambda)$ defined earlier. In Fig. 5 the theoretical (a-b) and experimental (c) interaction efficiencies (at the resonance wavelength) for the different antenna types are plotted. Each marker represents a certain DR (Fig. 5(a)) or BT (Fig. 5(b)) geometry (so a certain (H,Δ) combination; the width W of the DR antenna is again 55 nm and the bowtie apex angle $\alpha = 60°$). The gray line represents the SR interaction efficiency. The theoretical curves (Figs. 5(a) and 5(b)) predict that, for the same resonance wavelength λ_{res}, both DR and BT antennas generally have higher interaction efficiencies than SR antennas. The interaction efficiencies of DR antennas exceed the SR efficiencies $\eta_{SR}(\lambda_{res})$ by $30-50\%$ depending on the specific λ_{res} in the investigated wavelength region, while for BT antennas a typical increase between $20-40\%$ is observed. For a fixed λ_{res}, DR and BT antennas have an increased interaction efficiency when the gap Δ is larger (compared to the SR η). This is highlighted in the magnified parts of Figs. 5(a) and 5(b) respectively. The red markers correspond to a gap of $\Delta = 10$ nm while the purple markers correspond to $\Delta = 120$ nm. Differences up to 32% and 66% for DR and BT antennas respectively are observed. In Fig. 5(c) the experimental interaction efficiencies are plotted. The theoretically predicted trends are confirmed by our experiments. The interaction efficiencies of gapped nanoantennas generally exceed the SR efficiency while the larger gap structures generally have a higher η as compared

#228908 - $15.00 USD Received 5 Dec 2014; revised 18 Jan 2015; accepted 22 Jan 2015; published 2 Feb 2015

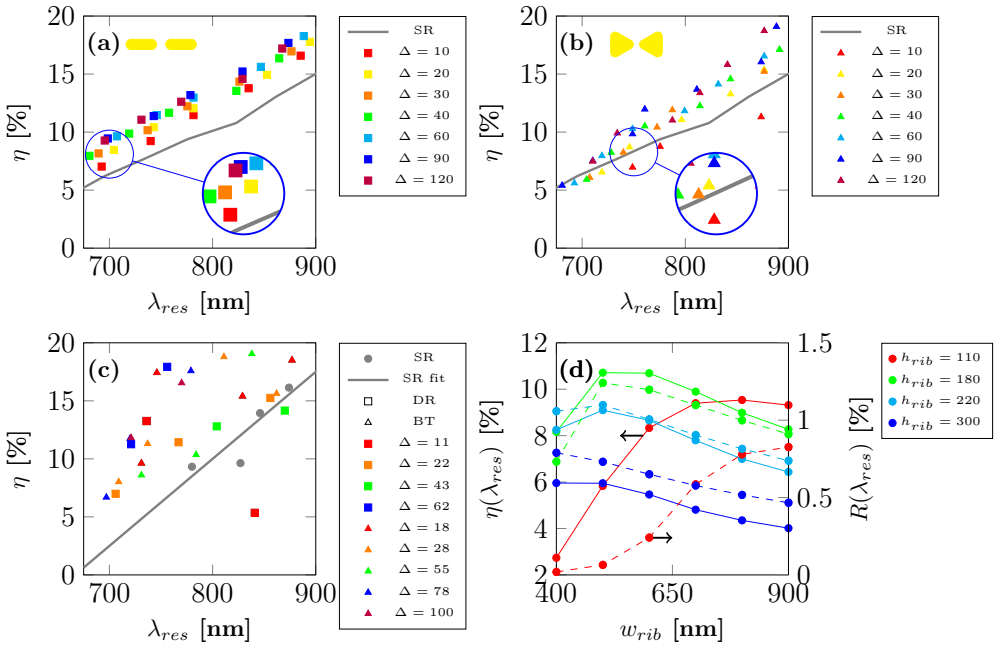

Fig. 5. **Comparison of interaction efficiencies. (a-b)** Theoretical interaction efficiencies $\eta(\lambda_{res})$ of DR **(a)** and BT **(b)** antennas as a function of the resonance wavelength λ_{res} compared with the SR interaction efficiency (gray line). Each color represents a certain gap: 10 nm (red), 20 nm (yellow), 30 nm (orange), 40 nm (green), 60 nm (cyan), 90 nm (blue), 120 nm (purple). For a given gap, an increasing λ_{res} corresponds with increasing H. **(c)** Experimental interaction efficiencies of DR (square markers) and BT (triangle markers) antennas compared with SR antennas (gray circles). The red, orange, green and blue square markers represent structures with gaps of 11 nm, 22 nm, 43 nm and 62 nm respectively while the red, orange, green, blue and purple triangle markers represent structures with gaps of 18 nm, 28 nm, 55 nm, 78 nm and 100 nm respectively. The gray line is a fit to the SR interaction efficiencies. **(d)** Theoretical interaction efficiency η (solid curves, left vertical axis) of a SR antenna ($H = 100$ nm and $W = 55$ nm) and power fraction R (dashed curves, right vertical axis) as a function of the waveguide width w_{rib} and height h_{rib} (both evaluated at λ_{res}).

#228908 - $15.00 USD Received 5 Dec 2014; revised 18 Jan 2015; accepted 22 Jan 2015; published 2 Feb 2015

to narrow gap structures (for the same λ_{res}). We report experimental interaction efficiencies as high as $\approx 19\%$ around 800 nm. Simulations show that the interaction efficiency decreases when the misalignment of the antenna with respect to the center of the waveguide increases. For the centro-symmetric antennas that we considered it is therefore always desirable that the misalignment between the two e-beamsteps is kept to a minimum in order to maximize the interaction efficiency with the evanescent field.

Apart from changing the antenna parameters to improve the interaction with the evanescent field, the waveguide geometry can also be adapted to optimize the interaction. For a fixed SR geometry ($H = 100$ nm, $W = 55$ nm and thickness $2+35+2 = 39$ nm) we varied the waveguide width w_{rib} for four waveguide thicknesses ($h_{rib} = 110, 180, 220, 300$ nm) and calculated $\eta(\lambda_{res})$ at the resonance wavelength λ_{res} for each (w_{rib}, h_{rib}) combination (see Fig. 5(d), solid curves expressed on the left vertical axis). For each h_{rib} an optimal width w_{rib} can be found for which η is maximized. When w_{rib} is decreased below a certain value (for a given h_{rib}) the waveguide mode goes into cut-off and hence causes a drop in η. The specific value of h_{rib} and w_{rib} has a negligible impact on the resonance wavelength λ_{res} but allows to change the spatial overlap between the excitation profile and the antenna cross-section by modifying the confinement of the waveguide mode. For an improved physical understanding we considered an unpatterned waveguide with varying width w_{rib} and height h_{rib} and calculated for each configuration the ratio $R(\lambda_{res})$ (again at λ_{res}) of the power flow through a cross-sectional area A_{ant} and the total modal power (where A_{ant} represents the cross-sectional area, perpendicular to the propagation direction, that would be covered by the antenna in case the waveguide would be patterned with it; for this particular SR case $A_{ant} = 100 \times 39$ nm^2). For each configuration this ratio hence represents the fraction of the modal power that flows through a fixed cross-sectional area that the antenna would cover in a plane perpendicular to the propagation direction. We found that $R(\lambda_{res})$ is maximized for the same (w_{rib}, h_{rib}) combination as the (w_{rib}, h_{rib}) combination that maximizes the interaction efficiency (see Fig. 5(d), dashed curves expressed on the right vertical axis). Physically this means that the optimal interaction efficiency is obtained when the fraction of the modal power that flows through the antenna cross-section is maximized.

5. Excitation of dark plasmon modes

Apart from the dipolar resonances considered so far, on-chip bowtie antennas allow higher order plasmon modes which can be excited when the apex angle is changed (Figs. 6(a) and 6(b)). In Fig. 6(a) the theoretical extinction spectra of a bowtie antenna with fixed height $H =$ 160 nm and gap $\Delta = 20$ nm but varying apex angle α are depicted. When α increases, the dipolar resonance redshifts, while a second blueshifted resonance appears for sufficiently large α. In order to reveal the nature of this resonance, the charge densities at the top surface of the $\alpha = 90^\circ$ BT antenna were simulated with Lumerical FDTD Solutions. The charge density is evaluated at the resonance of each peak, corresponding to $\lambda \approx 700$ nm (red dot in Fig. 6(a)) and $\lambda \approx 1125$ nm (green dot in Fig. 6(a)). Figures 6(c) and 6(d) represent the normalized charge density (the density is normalized with its maximum value) of the $\lambda = 700$ nm and $\lambda = 1125$ nm peak respectively. The $\lambda = 700$ nm resonance exhibits a quadrupolar nature while the $\lambda = 1125$ nm resonance corresponds to a dipolar charge distribution. The effective wavelength of the propagating waveguide mode is $\lambda/n_{eff} \approx 433nm$ (for $\lambda = 700$ nm) while the base of the BT antenna is $2H\tan(\alpha/2) = 320$ nm. In this case the quasi-static approximation no longer holds and phase delay effects become important. Since the antenna is not illuminated from the top but from the side, the phase of the excitation field changes considerably while the wave propagates along the antenna. The phase of the $y-$component of the excitation field (along the TE direction) is represented in Fig. 6(e) and plotted as a function of the propagation distance (and evaluated at the center of the waveguide patterned with the ($\alpha = 90^\circ$, $H = 160$

#228908 - $15.00 USD Received 5 Dec 2014; revised 18 Jan 2015; accepted 22 Jan 2015; published 2 Feb 2015

nm, $\Delta = 20$ nm) bowtie antenna). The blue dashed lines correspond to the outer tips of the bowtie antenna. The phase difference along the bowtie antenna is $< \pi$ for the dipole mode and $> \pi$ for the quadrupole mode. For the quadrupole mode the excitation field hence changes sign when propagating along the antenna. The waveguide mode can excite dark plasmon modes as soon as the apex angle α is large enough (allowing a substantial phase delay along the antenna), with an interaction efficiency of $\approx 15.62\%$ (for this particular BT antenna). When the height H (for fixed α) or the apex angle α (for fixed H) is increased, the dark resonance redshifts with concomitant increase in the interaction efficiency. It is interesting to note that waveguide excitation allows an equally efficient interaction of the evanescent field with the bright and the dark plasmon mode since the interaction efficiencies of both modes are of the same order (for a given λ_{res}). The excitation of a multipolar plasmon resonance is also experimentally verified and shown in Fig. 6(b) in which extinction spectra of BT antennas with different apex angles α are shown. The broad dipolar peak redshifts and a second resonance appears when α is increased. While the dipolar peak is again superimposed with a fringe pattern, the quadrupolar peak is much more smooth. Apart from a (partial) quenching of the radiative plasmon decay into the waveguide, the lack of fringes could also be explained by an anisotropic radiation pattern of the quadrupolar mode (e.g. predominant forward scattering and no backscattering along the waveguide mode propagation direction) or radiation along directions which don't couple back into the waveguide. Other antenna geometries, such as the nanocross [34], could be excited through an evanescent waveguide field in order to tailor specific and efficient on-chip multipolar plasmonic resonances which can be used for e.g. improved LSPR sensing. Furthermore, the multipole character of these gapped antennas could be applied for on-chip enhanced Raman spectroscopy by tuning the resonance peaks to optimally match both the pump and Stokes (or anti-Stokes) wavelength.

#228908 - $15.00 USD Received 5 Dec 2014; revised 18 Jan 2015; accepted 22 Jan 2015; published 2 Feb 2015

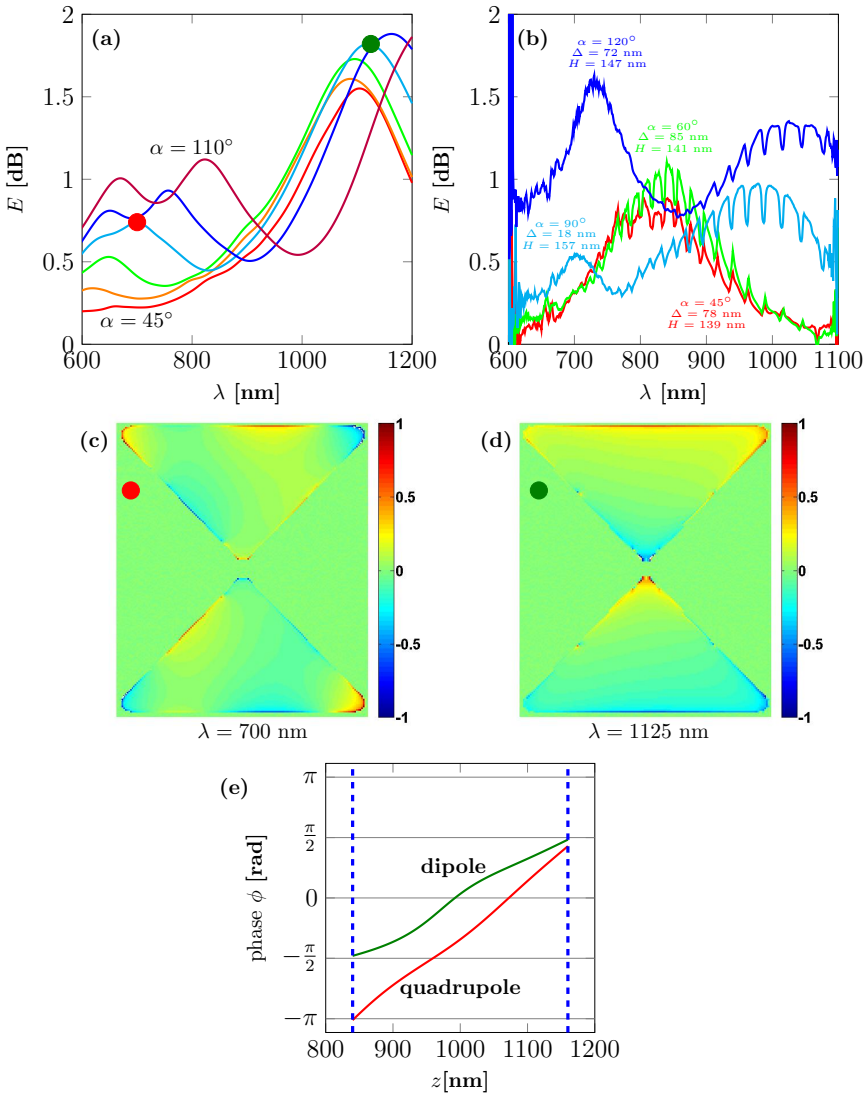

Fig. 6. **Multipole resonances. (a)** Theoretical extinction spectra of BT antennas with varying apex angle (45° (red), 60° (orange), 75° (green), 90° (cyan), 100° (blue), 110° (purple)) and fixed height $H = 160$ nm and gap $\Delta = 20$ nm. **(b)** Experimental extinction spectra of BT antennas with increasing apex angle: $\alpha = 45°$ (red), $\alpha = 60°$ (green), $\alpha = 90°$ (cyan) and $\alpha = 120°$ (blue). **(c-d)** Simulated charge density plots at the top surface of a BT antenna with height $H = 160$ nm, gap $\Delta = 20$ nm and apex angle $\alpha = 90°$. **(c)** Normalized charge density of the quadrupolar plasmon mode at $\lambda = 700$ nm (corresponding with the red dot in **(a)**). **(d)** Normalized charge density of the dipolar plasmon mode at $\lambda = 1125$ nm (corresponding with the green dot in **(a)**). **(e)** Phase of the y-component of the electric field as a function of the propagation distance (evaluated in the center of the waveguide cross-section). The blue dashed lines represent the outer tips of the bowtie antenna ($\alpha = 90°$, $H = 160$ nm, $\Delta = 20$ nm). The red line corresponds to the quadrupole mode (red dot in **(a)**) and the green line corresponds to the dipolar mode (green dot in **(a)**).

#228908 - $15.00 USD Received 5 Dec 2014; revised 18 Jan 2015; accepted 22 Jan 2015; published 2 Feb 2015

6. Conclusion

In conclusion, we have investigated an integrated nanoplasmonic platform in which three different antenna geometries (single rod, double rod and bowtie antenna) were fabricated on top of a single mode silicon nitride waveguide. The fabrication process, based on an ion milling of the lithographically defined nanoantennas, allows the fabrication of integrated narrow gap antennas (down to $\approx$ 10 nm) without having a detrimental impact on the waveguide losses (the best waveguide loss is $\approx$ 4 dB/cm at 785 nm). The theoretically predicted trends of how the resonance wavelength of single rod, double rod and bowtie antennas behaves under height, gap and angle changes upon evanescent waveguide excitation were confirmed by our experiments. Furthermore the interaction efficiencies of each antenna type were compared and it was shown that the waveguide geometry can be adapted, for a given antenna, in order to optimize the interaction between the evanescent field and the antenna. Experimental interaction efficiencies as high as $\approx$ 19% (around $\lambda \approx$ 800 nm) were measured for gapped nanostructures. Apart from the bright dipolar resonance we experimentally demonstrated the efficient excitation of an on-chip dark plasmon resonance in large apex bowtie antennas due to the propagation induced phase delay. This platform is suggested to be of potential interest for improved on-chip LSPR sensing and on-chip enhanced Raman spectroscopy.

Acknowledgments

We acknowledge Josine Loo (imec) for performing the e-beam lithography, Liesbet Van Landschoot (Ghent University) for making the SEM images and Ranjith Karuparambil Ramachandran (Ghent University) for the AFM measurement. F.P. acknowledges financial support from the Bijzonder Onderzoeksfonds of Ghent University (BOF) and the ERC grant InSpectra.

#228908 - $15.00 USD Received 5 Dec 2014; revised 18 Jan 2015; accepted 22 Jan 2015; published 2 Feb 2015